

Article

Ab Initio Study of Structure and Transport Properties of Warm Dense Nitric Oxide

Zhijian Fu ^{1,2,3}, Xianming Zhang ², Rui Wang ^{3,*}, Huayang Sun ⁴, Yangshun Lan ⁵, Jihong Xia ¹, Zhiguo Li ⁵ and Jing Song ⁶

¹ School of Electronic Information and Electrical Engineering, Chongqing University of Arts and Sciences, Chongqing 402160, China

² Engineering Research Center for Waste Oil Recovery Technology and Equipment, Ministry of Education, Chongqing Technology and Business University, Chongqing 400067, China

³ Department of Physics, Chongqing University, Chongqing 401331, China

⁴ Northwest Institute of Nuclear Technology, Xi'an 710024, China

⁵ National Key Laboratory for Shock Wave and Detonation Physics Research, Institute of Fluid Physics, Chinese Academy of Engineering Physics, Mianyang 621900, China

⁶ Institute of Process Engineering, Chinese Academy of Sciences, Beijing 100190, China

* Correspondence: rcwang@cqu.edu.cn

Abstract: The structure, equation of state and transport properties of warm dense nitric oxide (NO) were investigated in wide density and temperature ranges by ab initio molecular dynamics simulations. Both the Perdew–Burke–Ernzerhof (PBE) and the strongly constrained and appropriately normed functional with revised Vydrov–van Voorhis nonlocal correlation (SCAN–rVV10) functionals were used in the simulations, and the pressures predicted by the SCAN–rVV10 functional were found to be systematically lower than those predicted using PBE and experimental data along the shock Hugoniot curve. Along the Hugoniot curve, as density increased, we found that the system transformed towards a mixture of atomic nitrogen and oxygen liquids with molecular NO that remained present up to the highest densities explored. The electrical conductivity along Hugoniot indicated that nonmetal to metal transition had taken place. We also calculated the electrical and thermal conductivities of nitric oxide in the warm dense matter regime, and used them to compute the Lorentz number. In addition, we also report the electronic density of states.

Keywords: warm dense matter; nitric oxide; structure; ab initio simulations; transport properties



Citation: Fu, Z.; Zhang, X.; Wang, R.; Sun, H.; Lan, Y.; Xia, J.; Li, Z.; Song, J. Ab Initio Study of Structure and Transport Properties of Warm Dense Nitric Oxide. *Inorganics* **2022**, *10*, 120. <https://doi.org/10.3390/inorganics10080120>

Academic Editor: Koichiro Takao

Received: 17 July 2022

Accepted: 17 August 2022

Published: 18 August 2022

Publisher's Note: MDPI stays neutral with regard to jurisdictional claims in published maps and institutional affiliations.



Copyright: © 2022 by the authors. Licensee MDPI, Basel, Switzerland. This article is an open access article distributed under the terms and conditions of the Creative Commons Attribution (CC BY) license (<https://creativecommons.org/licenses/by/4.0/>).

1. Introduction

Materials under extreme conditions show unusual physical and chemical properties compared with normal conditions [1–5]. With the development of experimental and theoretical methods, materials under extreme conditions are studied widely. Shock loading technology is used to explore the equation of state of warm dense matter, which is useful for understanding detonation products and the interior of gas planets [2,6–8]. On the other hand, the method of ab initio molecular dynamics simulations (AIMD) [9] and path integral Monte Carlo (PIMC) [10] with supercomputer application make it possible to simulate different types of materials, such as, hydrogen [11–15], helium [16,17], oxygen [5,18,19], nitrogen [4,20–25], nitric oxide [24,26], ammonia [27–31], and methane [32].

Nitric oxide (NO) is part of the explosive compounds, and the principal Hugoniot equation of state (EOS) of NO is important for understanding the explosive process [24]. The NO system is as a calibration for the more complex H–C–N–O system [26,33]. NO also exists in star-forming regions [34]. Therefore, understanding the behavior of the NO system in a warm dense regime is important for the explosive process, shock compression experiments, and celestial evolution. The Hugoniot EOS of liquid NO was measured within the pressure range of 14–66 GPa by uniaxial shock wave technology [33]. Based

on quantum molecular dynamics simulations, the reaction process of liquid NO along the Hugoniot was analyzed, which indicated nitrogen molecules form when NO dissociates and oxygen remains in atomic form in the whole density–temperature range [26]. Then, the nonmetal–metal transition in fluid nitrogen oxide was observed at about 40 GPa by first principle molecular dynamics simulations [24]. However, the structure and transport properties of warm dense NO have still not been investigated systematically.

In the present work, the EOS and transport properties of warm dense NO were studied by ab initio molecular dynamics simulations. The Hugoniot EOS, pair correlation function (PCF), electrical conductivities, thermal conductivities, and Lorenz number were calculated in the warm dense matter regime. Based on the above analysis, the nonmetal–metal transition was investigated. At the same time, the density of states (DOS) of warm dense NO were shown.

2. Computational Method

2.1. Equation of State Calculations

The equation of state of warm dense NO was calculated at pressures up to 270 GPa using the Vienna ab initio simulation package (VASP) [35,36]. The present simulation was by the projector augmented wave (PAW) method [37]. Electronic exchange and correlation interactions were considered by the Perdew–Burke–Ernzerhof (PBE) [38] generalized gradient approximation (GGA) and the strongly constrained and appropriately normed functional with revised Vydrov–van Voorhis nonlocal correlation (SCAN–rVV10) functional [39,40], respectively. The calculations were performed for a canonical ensemble (NVT) with the conserved temperature, volume, and particle number in the cubic box within the Born–Oppenheimer approximation. The equal electron and ion temperatures based on local thermodynamic equilibrium were modeled by Fermi–Dirac distribution and Nosé–Hoover thermostats. The values $2s^22p^3$ and $2s^22p^4$ were considered in the pseudopotential for the valence electrons of nitrogen and oxygen, respectively. All the simulations were started using molecular NO as initial conditions. The simulations employed 27 NO molecules and relaxed 10–40 ps with 1.0 fs time step; at the same time, the Γ point and 1000 eV energy cutoff was used in the calculations. The number of bands was from 192 to 576 for 27 NO molecules in the temperature range of 122–43,070 K, and the number of bands in each calculation tested for thermal occupation was converged to better than 10^{-4} , which was equivalent to using 600 bands when simulating aluminum in a cell of 64 atoms at a temperature of 1 eV (1 eV = 11,604.522 K) [41].

2.2. Calculations for Transport Properties

The electrical and thermal conductivities were calculated using the Kubo–Greenwood formula [42–45],

$$\begin{aligned} \sigma &= L_{11}, \\ \kappa &= \frac{1}{e^2 T} \left(L_{22} - \frac{L_{12}^2}{L_{11}} \right), \\ L_{ij}(\omega) &= (-1)^{i+j} \frac{\hbar e^2}{V} \sum_{k',k} [f(\varepsilon_k) - f(\varepsilon_{k'})] \delta(\varepsilon_k - \varepsilon_{k'} - \hbar\omega) \\ &\quad \times \langle \psi_k | \hat{v} | \psi_{k'} \rangle \langle \psi_{k'} | \hat{v} | \psi_k \rangle (\varepsilon_k - \mu_e)^{i-1} (\varepsilon_{k'} - \mu_e)^{j-1}, \end{aligned} \quad (1)$$

where σ is electrical conductivity, κ is thermal conductivity, e is the electronic charge, T is the temperature, L_{ij} is Onsager kinetic coefficient, ω is the photon frequency of an external field, \hbar is the reduced Planck's constant, V is the volume of the cell, ε_k is the energy of eigenstate k , μ_e is the electronic chemical potential, \hat{v} is the velocity operator on the wave function, and $f(\varepsilon_k)$ is the occupation of the eigenstate of energy ε_k according to the Fermi occupation function. The electrical and thermal conductivity were obtained using *Abinit* code [46–49]. In the calculations of transport properties, we used 10 uncorrelated snapshots from AIMD simulation at every density and temperature with $2 \times 2 \times 2$ k points and PBE functional. The 480 to 800 bands were used in the calculation of transport properties.

The direct-current (dc) electrical and thermal conductivity was the zero-frequency limit of $\sigma(\omega)$ and $\kappa(\omega)$. The Lorentz number was computed by taking the ratio between the electrical and thermal conductivities, which was then compared to the Wiedemann–Franz law. The number of bands and k -points were carefully tested for convergence.

3. Results and Discussion

Before the calculations of EOS, 27 and 64 NO molecules were used to calculate the pressure and internal energy for testing the system–size convergence. Internal energy and pressure at 2.60 g cm^{-3} and 5947 K were $-9.25 \text{ eV/molecule}$, 39.2 GPa and $-9.27 \text{ eV/molecule}$, 38.9 GPa for 27 and 64 NO molecules, respectively. The error of internal energy and pressure was within 2% by comparing with the results of 27 NO and 64 NO in the density and temperature range studied. On the other hand, internal energy and pressure at 3.20 g cm^{-3} and 10,000 K were $-5.84364 \text{ eV/molecule}$ and 81.20 GPa considering the spin, and $-5.84114 \text{ eV/molecule}$ and 81.25 GPa without considering spin. The spin consideration in the simulations had a negligible effect on the pressure and internal energy. Therefore, 27 NO molecules and exclusion of spin were appropriate for the present simulation.

In order to obtain the Hugoniot of liquid NO, a series of calculations were implemented for different densities and temperatures. The internal energy E and pressure P were obtained by the calculations. Based on the Rankine–Hugoniot equation, $(E_H - E_0)$ and $(P_H + P_0)(V_0 - V_H)/2$ were calculated along different densities and temperatures, where V is volume, and subscripts 0 and H mean the initial and shock states, respectively. We solved the energy conservation Hugoniot equation, that is, when the difference between these two terms is zero, to obtain a state on the Hugoniot curve. An interpolation method was used to obtain temperatures and pressures when the difference was equal to 0. The obtained temperatures and pressures with density were along the Hugoniot state. Figure 1a shows the density and pressure line along the Hugoniot state of liquid nitric oxide compared with other experimental and theoretical results [24,26,33]. The initial state of liquid NO was set at a density of 1.263 g cm^{-3} and temperature of 122 K to correspond with the shock–compression experiment of Schott et al. [33]. PBE and SCAN–rVV10 were used in the present simulations. The present PBE pressures were in agreement with the shock–compression experimental data. On the other hand, the present SCAN–rVV10 calculations showed systematically underestimated pressures compared with the experimental data, even though the SCAN–rVV10 functional was designed to include the long–range interactions and preserve the short and intermediate–range description for the strongly constrained and appropriately normed functional (SCAN). The present PBE result agreed with the PW91 result calculated by Mazevet et al. [26]. Mazevet et al. used an initial state of 1.22 g cm^{-3} and 122 K, but they did not calculate the energy of this state using AIMD. Instead, they took the energy of an isolated NO molecule at an intermolecular distance of 2.175 Bohr. The present PBE pressure was in agreement with the result of Zhang et al. at a density lower than 3.30 g cm^{-3} , but was lower than that of Zhang et al. at a density higher than 3.30 g cm^{-3} [24], also shown in Table 1. A possible reason for the deviation is the different parameters used in the AIMD simulation, such as particle number, energy cutoff, and relaxation time. For the equation of state of higher densities and temperatures, the first–principles equation of state (FPEOS) code is a method to extract the EOS of the nitrogen–oxygen mixture from the EOS of a single element [3]. Figure 1c shows the pressures as a function of compression ratio (ρ/ρ_0) along the Hugoniot state. The present compression ratio reached 2.77, and we did not observe the phenomenon with nitrogen of the sharp change in slope along the Hugoniot state related to the dissociation [4]. One possible reason is the present compression ratio is not large enough and the sharp change in slope needs greater compression ratio. It should be noted that the initial state used by Zhang et al. was 0.807 g cm^{-3} and 122 K. The P – ρ/ρ_0 relationship of Zhang et al. showed different trends compared with other results. The present PBE and SCAN–rVV10 T – P lines were higher than those of Mazevet et al. and Zhang et al. as shown in Figure 1b, while the present PBE and SCAN–rVV10 ρ – T lines were lower than the results of Mazevet et al.

and Zhang et al. as shown in Figure 1d. Because the simulation using the SCAN–rVV10 functional showed the underestimated Hugoniot pressure compared with that of PBE, the PBE functional was mainly used for the calculation of the pair correlation functions and transport properties.

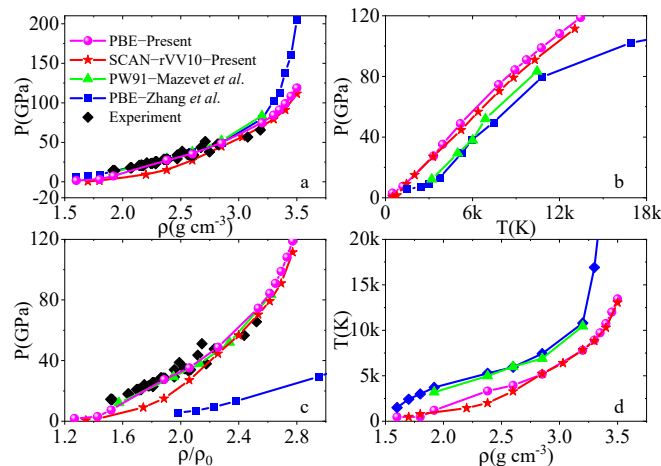


Figure 1. The Hugoniot curve of liquid nitric oxide ((a): pressure as a function of density, (b): pressure as a function of temperature, (c): pressure as a function of compression ratio, (d): temperature as function of density). The present calculation: magenta solid line with sphere for PBE functional and red solid line with star for SCAN–rVV10 functional both from the initial state at 1.263 g cm^{-3} and 122 K, compared with quantum molecular dynamics simulations (blue solid line with square for PBE functional of Zhang et al. from initial state at 0.807 g cm^{-3} and 122 K [24] and green solid line with triangle for PW91 functional of Mazevet et al. from initial state at 1.22 g cm^{-3} [26]) and experiment of Schott et al. (black diamond) [33].

Table 1. The present Hugoniot EOS compared with the results of Zhang et al. [24] and Mazevet et al. [26]; the density unit is g cm^{-3} , all temperature units are K, and all the pressure units are GPa.

Density	T_{PBE}	P_{PBE}	$T_{\text{SCAN-rVV10}}$	$P_{\text{SCAN-rVV10}}$	T_{Zhang}	P_{Zhang}	T_{Mazevet}	P_{Mazevet}
1.92	1203	7.4			3720	13.2	3194	12.1
2.38	3319	27.6	2003	15.0	5267	29.4	4979	29.3
2.60	3945	35.2	3286	27.1	5947	38.0	6000	37.9
2.85	5168	48.8	5222	44.7	7437	49.6	6890	52.0
3.20	7803	74.6	7853	70.4	10,794	79.6	10,452	83.4
3.30	8922	84.4	8828	79.2	16,903	102.1		
3.35	9723	91.0			22,451	112.4		
3.40	10,741	98.9	10,288	90.9	27,685	138.3		
3.45	12,004	108.3			30,000	160.0		
3.50	13,445	118.8	13,047	111.4	43,070	204.7		

Pair correlation function $g(r)$ is shown in Figure 2 and compared with the results of Zhang et al. and Mazevet et al. [24,26]. The present PCFs were obtained by using a visual molecular dynamics program (VMD) [50]. The present PCFs and those of Zhang et al. showed the same peak position but different heights. At lower density and temperature, the molecular peak at 1.15 \AA in the $g(r)_{\text{N-O}}$ indicated the existence of the nitric oxide molecules, while the molecular peak at 1.09 \AA in the $g(r)_{\text{N-N}}$ represented the existence of the nitrogen molecules. In Figure 2e,f, the present PCFs agreed with those of Mazevet et al. as shown in the figure, the PCFs of O–O at 1.20 \AA showed a very low peak, which indicated that oxygen mostly keeps in the atomic state in the whole density–temperature regime [26]. On the other hand, although the PW91 functional used in Mazevet’s work was different from the PBE functional used in the present calculation, the agreement of the PCFs between our and Mazevet’s was better than that of ours and Zhang’s, where PBE was also used in Zhang’s work. One possible reason for the difference of PCFs between ours and Zhang’s may be related to the difference of the calculation parameters expected in the functional used in the simulations. At the same time, the comparison of PCFs calculated using

different functionals are shown in Figure 3. The pair correlation function calculated using SCAN–rVV10 functional agreed with the result of the PBE functional.

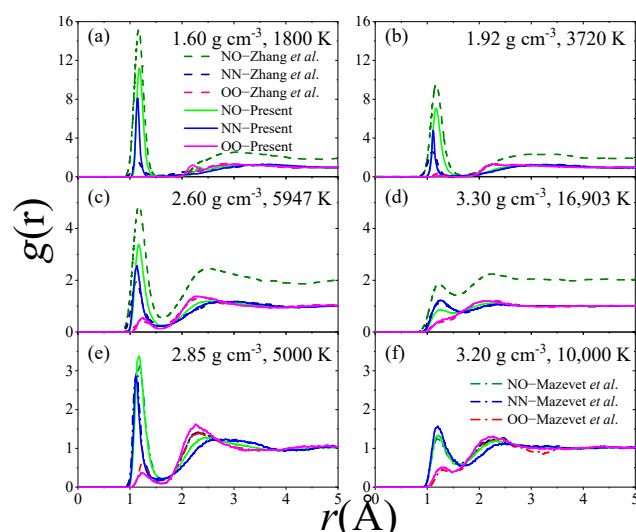


Figure 2. Pair correlation functions $g(r)$ for warm dense NO calculated by PBE functional at different densities and temperatures, compared with that of Zhang et al. [24] (a–d) and Mazevet et al. [26] (e,f).

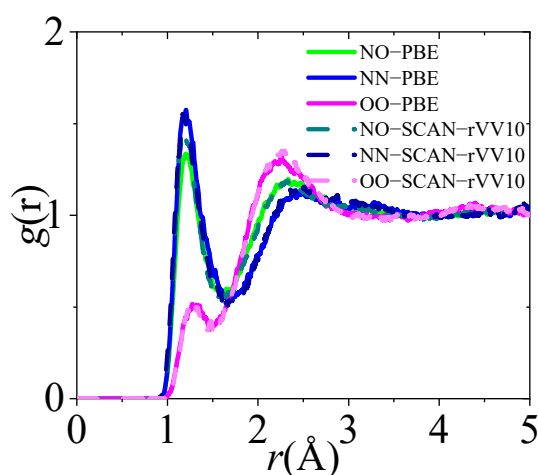


Figure 3. The present pair correlation functions at 3.20 g cm^{-3} and $10,000 \text{ K}$ calculated using PBE and SCAN–rVV10 functionals.

In order to quantitatively analyze the structure of warm dense nitric oxide, the short-range local structures were counted by the calculation of the bond length using the equilibrated configurations of AIMD simulations. The local structure contains atoms, molecules, and clusters. If the distance between two atoms is less than 2 times of the covalent radius, these two atoms are considered to be bonded. The covalent radius of atoms is calculated by the effective coordination number (ECN) model [51–53],

$$\begin{aligned} \text{ECN} &= \frac{1}{N} \sum_{i=1}^N \text{ECN}_i = \frac{1}{N} \sum_{i=1}^N \sum_{j=1}^N \exp\left[1 - \left(\frac{d_{ij}}{d_{av}^i}\right)^6\right], \\ d_{av}^i &= \frac{\sum_j d_{ij} \exp\left[1 - \left(\frac{d_{ij}}{d_{av}^i}\right)^6\right]}{\sum_j \exp\left[1 - \left(\frac{d_{ij}}{d_{av}^i}\right)^6\right]}, \\ d_{av} &= \frac{1}{N} \sum_{i=1}^N d_{av}^i, \end{aligned} \quad (2)$$

where i and j are the indices of the nitrogen or oxygen atom, d_{ij} is the distance between the i th atom and the j th atom, d_{av}^i is calculated self-consistently within three to four iterations [51], and $d_{av}/2$ is the covalent radius of the atom. As an example, one structure at 2.85 g cm^{-3} and 5168 K calculated using PBE functional is shown in Figure 4. Red spheres represent oxygen atoms, while blue spheres for nitrogen atoms. As shown in the figure, nitrogen and oxygen atoms, NO molecules, nitrogen and oxygen molecules, and N_2O coexist.

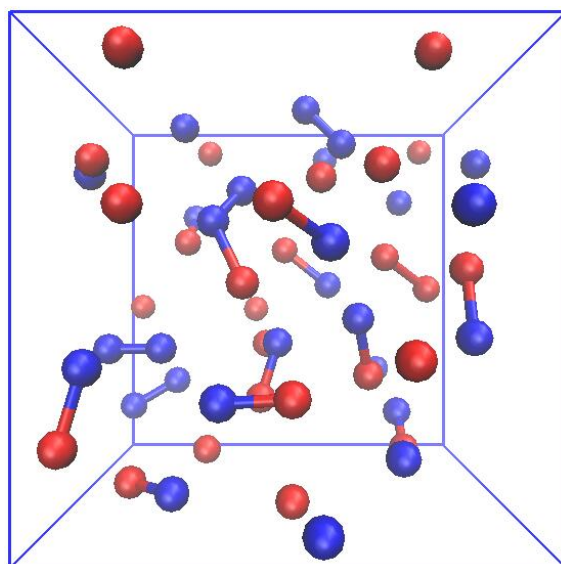


Figure 4. Snapshot of the AIMD simulation at 2.85 g cm^{-3} and 5168 K from the AIMD calculation using 27NO molecules and PBE functional, red and blue spheres represent oxygen and nitrogen atoms, respectively.

Figure 5 shows fractions of different components in warm dense nitric oxide along the Hugoniot curve. As shown in the figure, the main components were NO molecules, O atoms, and N atoms, which was consistent with Mazevet's findings [26]. The dissociation of NO molecules is related with the nonmetal to metal transition. On the other hand, there are N_2 , O_2 , N_2O , NO_2 , and O_3 in warm dense nitric oxide, which comes from the recombination of nitrogen and oxygen atoms due to temperature and pressure effects.

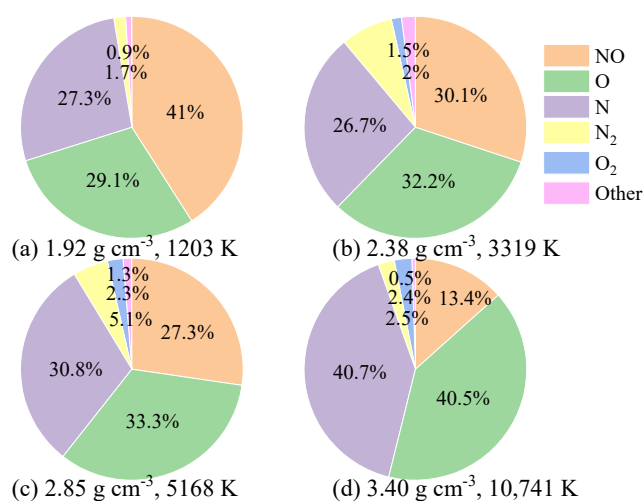


Figure 5. Fractions of components in warm dense NO along Hugoniot using PBE functional. The components contain NO molecules, N and O atoms, N_2 and O_2 molecules, and Other.

The direct current (dc) conductivity was obtained as the static limit of dynamic conductivity. The dynamic conductivity was calculated by *Abinit* using the Kubo–Greenwood formula [42,43], and also the dc conductivity was directly obtained by *Abinit*. In local thermodynamic equilibrium, 10 independent equilibrated ionic configurations are used for calculating electrical conductivity [46–49]. The present result of electrical conductivity was in agreement with that of Zhang et al. as shown in Figure 6. The electrical conductivity reached 10^5 S m^{-1} at pressure higher than 40 GPa, which indicated liquid nitric oxide had reached a metallic state.

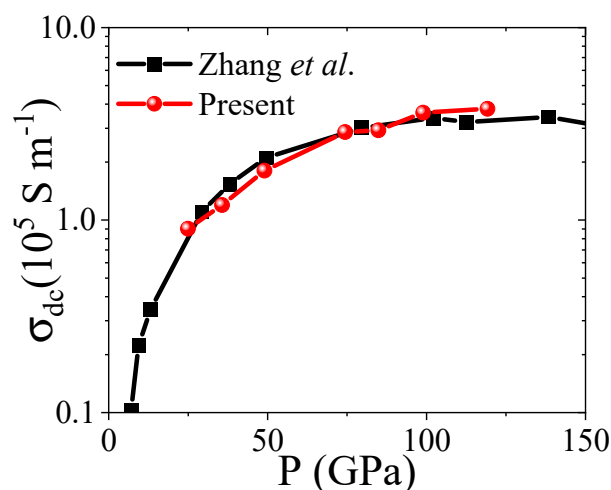


Figure 6. The direct current conductivities σ_{dc} using PBE functional along the Hugoniot curve, compared with the result of Zhang et al. [24].

The comparison of the dc conductivity with nitrogen–oxygen 1:1 mixture at 2000 K is shown in Figure 7 [54]. The dc conductivity of NO system was higher than the N–O mixture system at the same pressure. Those two systems are different from the dissociation process. In the NO system, the NO molecules dissociate nitrogen and oxygen atoms, while nitrogen and oxygen atoms come from nitrogen and oxygen molecules in the N–O mixture system. The difference in the dc conductivities with pressure may associate with the different dissociation process.

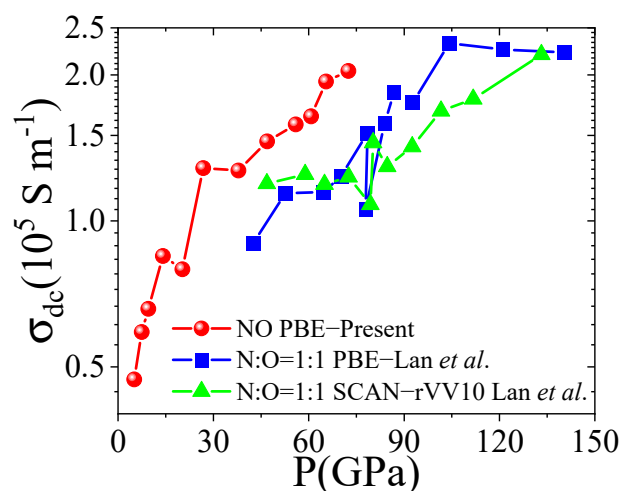


Figure 7. The direct current conductivities of NO along 2000 K isotherm, compared with the result of the nitrogen–oxygen 1:1 mixture at 2000 K calculated by Lan et al. [54].

The dc conductivity of warm dense NO is shown as a function of density along 2000 K, 5000 K, 10,000 K, and Hugoniot in Figure 8. As shown in the figure, the electrical conductivity increased with the increasing densities along different temperatures and the

Hugoniot. The electrical conductivity increased with the increasing temperatures in the whole density range. In the density range of $1.50\text{--}3.50\text{ g cm}^{-3}$, the electrical conductivity changed from 0.5×10^5 to $4.0 \times 10^5\text{ S m}^{-1}$ and it demonstrated liquid NO was in the metallic state.

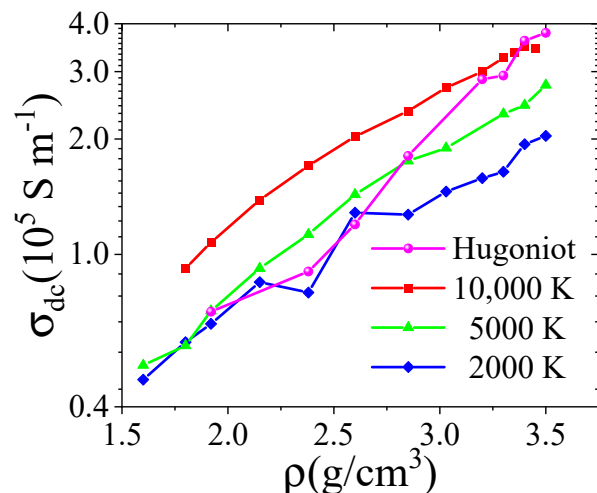


Figure 8. The dc conductivity σ_{dc} of warm dense NO as a function of density along different isotherms and the principal Hugoniot using PBE functional.

The phonon and electron contribution to the thermal conductivity was different for different materials [55]. Due to the metallic state of the liquid NO studied, the electronic thermal conductivity, calculated using Equation (1), is shown as a function of density along the same isotherms and Hugoniot as the electrical conductivity in Figure 9. With increasing density, the thermal conductivity increased along all the isotherms and the Hugoniot studied. When temperature was lower than 5000 K, the increase in the thermal conductivity was mainly attributed to the density effect. On the other hand, compared with the PCFs of liquid NO, with increasing density and temperature, NO molecules dissociated company with the increase in delocalized electrons and because of the thermal excitation, thermal conductivity gradually increased.

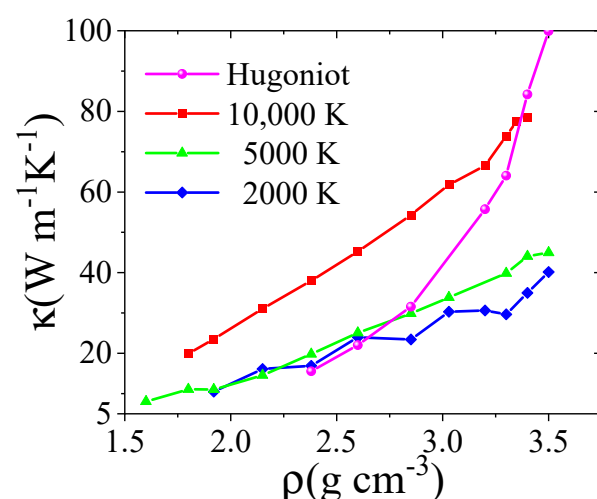


Figure 9. Thermal conductivity κ of warm dense NO along isotherms and the principal Hugoniot using PBE functional.

The Lorenz number connects with electrical and thermal conductivity. The ratio of thermal conductivity and electrical conductivity for metal at a given temperature is usually assumed to be a constant, which is known as the Wiedemann–Franz law. The Lorenz

number is $L_0 = 2.44 \times 10^{-8} \text{ W } \Omega \text{ K}^{-2}$ for simple metal. We investigated the validity of the Wiedemann–Franz law for warm dense nitric oxide in the whole density and temperature range studied, as shown in Figure 10. The Lorenz number along Hugoniot at a density lower than 2.50 g cm^{-3} changed from $44.8 \times 10^{-8} \text{ W } \Omega \text{ K}^{-2}$ to $4.7 \times 10^{-8} \text{ W } \Omega \text{ K}^{-2}$, which showed large deviations from the Wiedemann–Franz law. The difference with the Wiedemann–Franz law along Hugoniot may be related to the dissociation of nitric oxide and the nonmetal–metal transition. The Lorenz number along 2000 K isotherm was about $10^{-7} \text{ W } \Omega \text{ K}^{-2}$, which indicated warm dense NO could not be regarded as a simple metal, although the electrical conductivity at 2000 K in the density range of $1.80\text{--}3.50 \text{ g cm}^{-3}$ reached $0.5 \times 10^5\text{--}2.0 \times 10^5 \text{ S m}^{-1}$. The deviations from the Wiedemann–Franz law were also observed in the warm dense hydrogen and nitrogen system [20,56]. However, the Wiedemann–Franz law is valid at very high densities (beyond 3.0 g cm^{-3}) when the temperature is higher than 5000 K. The fact that the value of L changes with pressure and temperature shows that the Wiedemann–Franz law is not always valid, in other words, the ratio between thermal and electrical conductivity is not constant, but depends on both temperature and density.

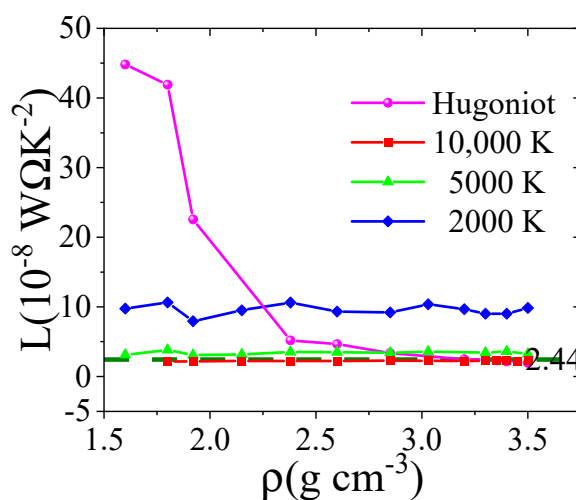


Figure 10. Lorenz number L of warm dense NO along isotherms and the principal Hugoniot using PBE functional. The olive dash line corresponds to $L_0 = 2.44 \times 10^{-8} \text{ W } \Omega \text{ K}^{-2}$.

In order to understand the metallic state of warm dense nitric oxide, the electric density of states of NO along different densities and temperatures are shown in Figure 11. The DOS of NO was obtained from VASP by averaging over 10 uncorrelated snapshots chosen from the AIMD simulations with 27 NO molecules and $7 \times 7 \times 7$ k -point grid with Gaussian smearing of 0.01 eV. As shown in the figure, the band gap was closed at a density of 1.92 g cm^{-3} and temperature of 2000 K, which is consistent with the electrical conductivity on the magnitude order of 10^5 S m^{-1} in Figure 5. With the increasing densities and temperatures, the electric DOS gradually moved to the Fermi level. At the same time, the partial density of states at 1.92 g cm^{-3} and 2000 K is shown in Figure 12. As shown in the figure, the 2s orbitals of nitrogen and oxygen were mainly in the range of $-30\text{--}20 \text{ eV}$, while the 2p orbitals of nitrogen and oxygen were close to Fermi level.

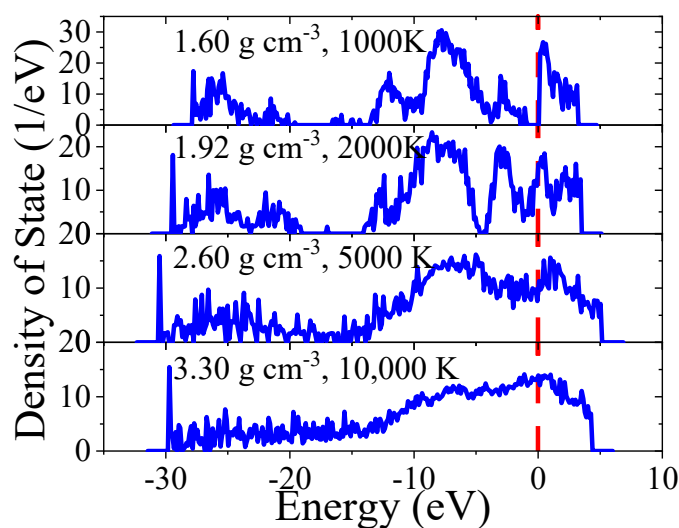


Figure 11. Electric density of states of warm dense nitric oxide at different densities and temperatures using PBE functional. The Fermi level is shown as the red dashed line.

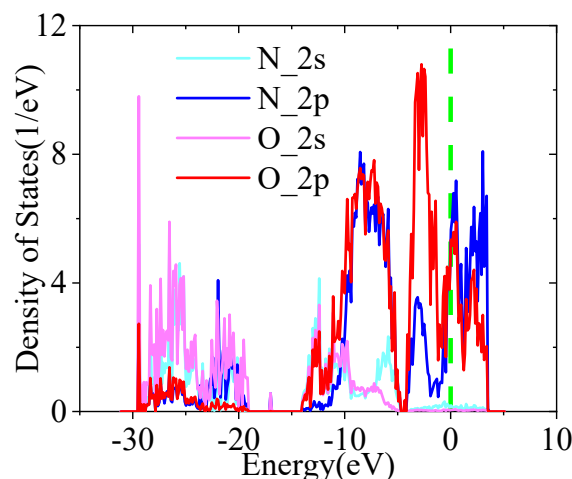


Figure 12. The partial density of states of NO at 1.92 g cm^{-3} and 2000 K using PBE functional. The Fermi level is shown as the green dashed line.

4. Conclusions

We employed ab initio molecular dynamics simulations to calculate the equation of state and transport properties of warm dense nitric oxide up to 200 GPa. The EOS of SCAN-rVV10 along Hugoniot showed relatively underestimated results compared with shock compression experimental data and that of PBE. The pair correlation functions indicated that nitric oxide gradually dissociates and oxygen remains in an atomic state. The electrical conductivity along Hugoniot indicated the nonmetal to metal transition at pressure above 40 GPa. The electrical and thermal conductivity increased with density in the whole density and temperature range studied. The Lorenz number at 2000 K and density lower than 2.50 g cm^{-3} along Hugoniot did not conform to the Wiedemann–Franz law, which is related to dissociation and nonmetal to metal transition. The density of states of warm dense nitric oxide were investigated for an understanding of the metallic state.

Author Contributions: The major work for this article, designing, execution and writing of the original draft, was done by the first author Z.F. Data curation, H.S., Y.L. and Z.L.; review and editing, R.W. and X.Z.; The other authors, J.X. and J.S., were responsible for supervision, editing, and reviewing of this article. All authors have read and agreed to the published version of the manuscript.

Funding: This work has been supported by the National Natural Science Foundation of China (Grant Nos. 11804037, 12174357, 12147102), the Foundation and Frontier Research Project of Chongqing (cstc2018jcyjAX0348), the Scientific and Technological Research Program of the Chongqing Municipal Education Commission (Grant No. KJZD–M201900802), and by the Fundamental Research Funds for the Central Universities under Grant No. 2020CDJQY–Z003.

Institutional Review Board Statement: Not applicable.

Informed Consent Statement: Not applicable.

Data Availability Statement: Not applicable.

Acknowledgments: We thank China Postdoctoral Program.

Conflicts of Interest: The authors declare no conflict of interest.

References

1. Jourdain, N.; Lecherbourg, L.; Recoules, V.; Renaudin, P.; Dorchie, F. Ultrafast Thermal Melting in Nonequilibrium Warm Dense Copper. *Phys. Rev. Lett.* **2021**, *126*, 065001. [[CrossRef](#)] [[PubMed](#)]
2. Guarguaglini, M.; Soubiran, F.; Hernandez, J.A.; Benuzzi-Mounaix, A.; Bolis, R.; Brambrink, E.; Vinci, T.; Ravasio, A. Electrical conductivity of warm dense silica from double-shock experiments. *Nat. Commun.* **2021**, *12*, 840. [[CrossRef](#)] [[PubMed](#)]
3. Militzer, B.; Gonzalez-Cataldo, F.; Zhang, S.; Driver, K.P.; Soubiran, F. First-principles equation of state database for warm dense matter computation. *Phys. Rev. E* **2021**, *103*, 013203. [[CrossRef](#)] [[PubMed](#)]
4. Driver, K.P.; Militzer, B. First-principles equation of state calculations of warm dense nitrogen. *Phys. Rev. B* **2016**, *93*, 064101. [[CrossRef](#)]
5. Driver, K.P.; Soubiran, F.; Zhang, S.; Militzer, B. First-principles equation of state and electronic properties of warm dense oxygen. *J. Chem. Phys.* **2015**, *143*, 164507. [[CrossRef](#)]
6. Tracy, S.J.; Turneure, S.J.; Duffys, T.S. In situ X-Ray Diffraction of Shock-Compressed Fused Silica. *Phys. Rev. Lett.* **2018**, *120*, 135702. [[CrossRef](#)]
7. Millot, M.; Hamel, S.; Rygg, J.R.; Celliers, P.M.; Collins, G.W.; Coppari, F.; Fratanduono, D.E.; Jeanloz, R.; Swift, D.C.; Eggert, J.H. Experimental evidence for superionic water ice using shock compression. *Nat. Phys.* **2018**, *14*, 297–302. [[CrossRef](#)]
8. Li, Z.-G.; Chen, Q.-F.; Gu, Y.-J.; Zheng, J.; Zhang, W.; Liu, L.; Li, G.-J.; Wang, Z.-Q.; Dai, J.-Y. Multishock compression of dense cryogenic hydrogen-helium mixtures up to 60 GPa: Validating the equation of state calculated from first principles. *Phys. Rev. B* **2018**, *98*, 064101. [[CrossRef](#)]
9. Hu, S.X.; Militzer, B.; Collins, L.A.; Driver, K.P.; Kress, J.D. First-principles prediction of the softening of the silicon shock Hugoniot curve. *Phys. Rev. B* **2016**, *94*, 094109. [[CrossRef](#)]
10. Militzer, B.; Driver, K.P. Development of Path Integral Monte Carlo Simulations with Localized Nodal Surfaces for Second-Row Elements. *Phys. Rev. Lett.* **2015**, *115*, 176403. [[CrossRef](#)]
11. Ma, Q.; Dai, J.; Kang, D.; Murillo, M.S.; Hou, Y.; Zhao, Z.; Yuan, J. Extremely Low Electron-ion Temperature Relaxation Rates in Warm Dense Hydrogen: Interplay between Quantum Electrons and Coupled Ions. *Phys. Rev. Lett.* **2019**, *122*, 015001. [[CrossRef](#)]
12. Schöttler, M.; Redmer, R. Ab Initio Calculation of the Miscibility Diagram for Hydrogen-Helium Mixtures. *Phys. Rev. Lett.* **2018**, *120*, 115703. [[CrossRef](#)]
13. Monserrat, B.; Drummond, N.D.; Dalladay-Simpson, P.; Howie, R.T.; Lopez Rios, P.; Gregoryanz, E.; Pickard, C.J.; Needs, R.J. Structure and Metallicity of Phase V of Hydrogen. *Phys. Rev. Lett.* **2018**, *120*, 255701. [[CrossRef](#)]
14. Mazzola, G.; Helled, R.; Sorella, S. Phase Diagram of Hydrogen and a Hydrogen-Helium Mixture at Planetary Conditions by Quantum Monte Carlo Simulations. *Phys. Rev. Lett.* **2018**, *120*, 025701. [[CrossRef](#)]
15. Borinaga, M.; Ibanez-Azpiroz, J.; Bergara, A.; Errea, I. Strong Electron-Phonon and Band Structure Effects in the Optical Properties of High Pressure Metallic Hydrogen. *Phys. Rev. Lett.* **2018**, *120*, 057402. [[CrossRef](#)]
16. Preising, M.; Redmer, R. High-pressure melting line of helium from ab initio calculations. *Phys. Rev. B* **2019**, *100*, 184107. [[CrossRef](#)]
17. Preising, M.; Lorenzen, W.; Becker, A.; Redmer, R.; Knudson, M.D.; Desjarlais, M.P. Equation of state and optical properties of warm dense helium. *Phys. Plasmas* **2018**, *25*, 012706. [[CrossRef](#)]
18. Sun, J.; Martinez-Canales, M.; Klug, D.D.; Pickard, C.J.; Needs, R.J. Persistence and eventual demise of oxygen molecules at terapascal pressures. *Phys. Rev. Lett.* **2012**, *108*, 045503. [[CrossRef](#)]
19. Bastea, M.; Mitchell, A.; Nellis, W. High Pressure Insulator-Metal Transition in Molecular Fluid Oxygen. *Phys. Rev. Lett.* **2001**, *86*, 3108–3111. [[CrossRef](#)]
20. Fu, Z.; Chen, Q.; Li, Z.; Tang, J.; Zhang, W.; Quan, W.; Li, J.; Zheng, J.; Gu, Y. Ab initio study of the structures and transport properties of warm dense nitrogen. *High Energy Density Phys.* **2019**, *31*, 52–58. [[CrossRef](#)]
21. Zhao, G.; Wang, H.; Ding, M.C.; Zhao, X.G.; Wang, H.Y.; Yan, J.L. Stability line of liquid molecular nitrogen based on the SCAN meta-GGA density functional. *Phys. Rev. B* **2018**, *98*, 184205. [[CrossRef](#)]

22. Cormier, M.M.E.; Bonev, S.A. Polymerization of sodium-doped liquid nitrogen under pressure. *Phys. Rev. B* **2017**, *96*, 184104. [[CrossRef](#)]
23. Tomasino, D.; Kim, M.; Smith, J.; Yoo, C.-S. Pressure-Induced Symmetry-Lowering Transition in Dense Nitrogen to Layered Polymeric Nitrogen (LP-N) with Colossal Raman Intensity. *Phys. Rev. Lett.* **2014**, *113*, 205502. [[CrossRef](#)]
24. Zhang, Y.; Wang, C.; Zheng, F.; Zhang, P. Quantum molecular dynamics simulations for the nonmetal-metal transition in fluid nitrogen oxide. *J. Appl. Phys.* **2012**, *112*, 033501. [[CrossRef](#)]
25. Boates, B.; Bonev, S. First-Order Liquid-Liquid Phase Transition in Compressed Nitrogen. *Phys. Rev. Lett.* **2009**, *102*, 015701. [[CrossRef](#)]
26. Mazevet, S.; Blottiau, P.; Kress, J.; Collins, L. Quantum molecular dynamics simulations of shocked nitrogen oxide. *Phys. Rev. B* **2004**, *69*, 224207. [[CrossRef](#)]
27. Naden Robinson, V.; Wang, Y.; Ma, Y.; Hermann, A. Stabilization of ammonia-rich hydrate inside icy planets. *Proc. Natl. Acad. Sci. USA* **2017**, *114*, 9003–9008. [[CrossRef](#)]
28. Liu, C.; Mafety, A.; Queyroux, J.A.; Wilson, C.W.; Zhang, H.; Beneut, K.; Le Marchand, G.; Baptiste, B.; Dumas, P.; Garbarino, G.; et al. Topologically frustrated ionisation in a water-ammonia ice mixture. *Nat. Commun.* **2017**, *8*, 1065. [[CrossRef](#)]
29. Jiang, X.; Wu, X.; Zheng, Z.; Huang, Y.; Zhao, J. Ionic and superionic phases in ammonia dihydrate NH₃·2H₂O under high pressure. *Phys. Rev. B* **2017**, *95*, 144104. [[CrossRef](#)]
30. Muñoz Caro, G.M.; Dartois, E.; Boduch, P.; Rothard, H.; Domaracka, A.; Jiménez-Escobar, A. Comparison of UV and high-energy ion irradiation of methanol:ammonia ice. *Astron. Astrophys.* **2014**, *566*, A93. [[CrossRef](#)]
31. Ninet, S.; Datchi, F.; Saitta, A.M. Proton disorder and superionicity in hot dense ammonia ice. *Phys. Rev. Lett.* **2012**, *108*, 165702. [[CrossRef](#)] [[PubMed](#)]
32. Li, D.; Zhang, P.; Yan, J. Quantum molecular dynamics simulations for the nonmetal-metal transition in shocked methane. *Phys. Rev. B* **2011**, *84*, 184204. [[CrossRef](#)]
33. Schott, G.L.; Shaw, M.S.; Johnson, J.D. Shocked states from initially liquid oxygen–nitrogen systems. *J. Chem. Phys.* **1985**, *82*, 4264–4275. [[CrossRef](#)]
34. Ziurys, L.M.; McGonagle, D.; Minh, Y.; Irvine, W.M. Nitric Oxide in Star-forming Regions: Further Evidence for Interstellar N–O Bonds. *Astrophys. J.* **1991**, *373*, 535. [[CrossRef](#)]
35. Kresse, G.; Joubert, D. From ultrasoft pseudopotentials to the projector augmented-wave method. *Phys. Rev. B* **1999**, *59*, 1758–1775. [[CrossRef](#)]
36. Kresse, G.; Furthmüller, J. Efficient iterative schemes for ab initio total-energy calculations using a plane-wave basis set. *Phys. Rev. B* **1996**, *54*, 11169–11186. [[CrossRef](#)]
37. Blöchl, P.E. Projector augmented-wave method. *Phys. Rev. B* **1994**, *50*, 17953–17979. [[CrossRef](#)]
38. Perdew, J.P.; Burke, K.; Ernzerhof, M. Generalized Gradient Approximation Made Simple. *Phys. Rev. Lett.* **1996**, *77*, 3865–3868. [[CrossRef](#)]
39. Peng, H.; Yang, Z.-H.; Perdew, J.P.; Sun, J. Versatile van der Waals Density Functional Based on a Meta-Generalized Gradient Approximation. *Phys. Rev. X* **2016**, *6*, 041005. [[CrossRef](#)]
40. Sun, J.; Remsing, R.C.; Zhang, Y.; Sun, Z.; Ruzsinszky, A.; Peng, H.; Yang, Z.; Paul, A.; Waghmare, U.; Wu, X.; et al. Accurate first-principles structures and energies of diversely bonded systems from an efficient density functional. *Nat. Chem.* **2016**, *8*, 831–836. [[CrossRef](#)]
41. Blanchet, A.; Torrent, M.; Cléroutin, J. Requirements for very high temperature Kohn–Sham DFT simulations and how to bypass them. *Phys. Plasmas* **2020**, *27*, 122706. [[CrossRef](#)]
42. Kubo, R. Statistical-mechanical theory of irreversible processes: I. General theory and simple applications to magnetic and conduction problems. *J. Phys. Soc. Jpn.* **1957**, *12*, 570–586. [[CrossRef](#)]
43. Greenwood, D.A. The Boltzmann equation in the theory of electrical conduction in metals. *Proc. Phys. Soc.* **1958**, *71*, 585. [[CrossRef](#)]
44. Pozzo, M.; Desjarlais, M.P.; Alfè, D. Electrical and thermal conductivity of liquid sodium from first-principles calculations. *Phys. Rev. B* **2011**, *84*, 054203. [[CrossRef](#)]
45. Mazevet, S.; Torrent, M.; Recoules, V.; Jollet, F. Calculations of the transport properties within the PAW formalism. *High Energy Density Phys.* **2010**, *6*, 84–88. [[CrossRef](#)]
46. Gonze, X.; Amadon, B.; Antonius, G.; Arnardi, F.; Baguet, L.; Beuken, J.-M.; Bieder, J.; Bottin, F.; Bouchet, J.; Bousquet, E.; et al. The Abinitproject: Impact, environment and recent developments. *Comput. Phys. Commun.* **2020**, *248*, 107042. [[CrossRef](#)]
47. Gonze, X.; Amadon, B.; Anglade, P.M.; Beuken, J.M.; Bottin, F.; Boulanger, P.; Bruneval, F.; Caliste, D.; Caracas, R.; Côté, M. ABINIT: First-principles approach to material and nanosystem properties. *Comput. Phys. Commun.* **2009**, *180*, 2582–2615. [[CrossRef](#)]
48. Gonze, X. A brief introduction to the ABINIT software package. *Z. Krist.-Cryst. Mater.* **2005**, *220*, 558–562. [[CrossRef](#)]
49. Gonze, X.; Beuken, J.M.; Caracas, R.; Detraux, F.; Fuchs, M.; Rignanese, G.M.; Sindic, L.; Verstraete, M.; Zerah, G.; Jollet, F. First-principles computation of material properties: The ABINIT software project. *Comput. Mater. Sci.* **2002**, *25*, 478–492. [[CrossRef](#)]
50. Humphrey, W.; Dalke, A.; Schulten, K. VMD: Visual molecular dynamics. *J. Mol. Graph.* **1996**, *14*, 33–38. [[CrossRef](#)]

51. Piotrowski, M.J.; Piquini, P.; Da Silva, J.L.F. Density functional theory investigation of 3d, 4d, and 5d 13-atom metal clusters. *Phys. Rev. B* **2010**, *81*, 155446. [[CrossRef](#)]
52. Sun, H.; Kang, D.; Dai, J.; Zeng, J.; Yuan, J. Quantum molecular dynamics study on the structures and dc conductivity of warm dense silane. *Phys. Rev. E* **2014**, *89*, 022128. [[CrossRef](#)] [[PubMed](#)]
53. Dai, J.; Hou, Y.; Yuan, J. Influence of ordered structures on electrical conductivity and XANES from warm to hot dense matter. *High Energy Density Phys.* **2011**, *7*, 84–90. [[CrossRef](#)]
54. Lan, Y.-S.; Wang, Z.-Q.; Liu, L.; Li, G.-J.; Sun, H.-Y.; Fu, Z.-J.; Gu, Y.-J.; Yang, G.; Li, L.-N.; Li, Z.-G.; et al. First-order liquid-liquid phase transition in nitrogen–oxygen mixtures. *Phys. Rev. B* **2021**, *103*, 144105. [[CrossRef](#)]
55. Deng, J.; Stixrude, L. Thermal Conductivity of Silicate Liquid Determined by Machine Learning Potentials. *Geophys. Res. Lett.* **2021**, *48*, e2021GL093806. [[CrossRef](#)]
56. Holst, B.; French, M.; Redmer, R. Electronic transport coefficients from ab initio simulations and application to dense liquid hydrogen. *Phys. Rev. B* **2011**, *83*, 235120. [[CrossRef](#)]